RSC Advances

PAPER

View Article Online
View Journal | View Issue

Cite this: *RSC Adv.*, 2020, **10**, 34943

Received 28th July 2020
Accepted 12th September 2020

DOI: 10.1039/d0ra06529c

rsc.li/rsc-advances

Synthesis and characterization of MOFs constructed from 5-(benzimidazole-1-yl) isophthalic acid and highly selective fluorescence detection of Fe(III) and Cr(VI) in water†

Bin Zhu,[b] Guimei Huang,[a] Yanni He,[a] Jisheng Xie,[a] Tao He,[a] Junli Wang*[a] and Ziao Zong *[a]

In this work, four novel metal–organic frameworks $[Cd(bipa)]_n$ (**1**), $\{[Zn_2(bipa)_2]\cdot 2C_2H_5OH\}_n$ (**2**), $\{[Co(bipa)]\cdot C_2H_5OH\}_n$ (**3**), $\{[Ni(bipa)_2]\cdot 2DMA\}_n$ (**4**), (H_2bipa = 5-(benzimidazole-1-yl)isophthalic acid) were successfully synthesized under solvothermal conditions. Complexes **1–4** were characterized by powder X-ray diffraction, elemental analysis, infrared spectroscopy and thermogravimetric analysis. Interestingly, the coordination patterns and 3D network structures of complexes **1–3** are very similar, while complex **4** is relatively unique. Complexes **1–2** exhibit potential fluorescent properties. Complex **1** can selectively and sensitively detect trace Fe(III) and Cr(VI) in water by fluorescence quenching detection, and the quenching mechanism is further discussed.

1. Introduction

Metal ions have played an extremely important role in industrial production and biological metabolism.[1] Chromium is an indispensable metal material in leather production, electroplating, printing and dyeing, metallurgy and in the nuclear industry.[2–6] A large amount of chromium ions are discharged into rivers with industrial wastewater, which seriously affects the ecological environment and human health. Chromium ions with different chemical valences have different physical and biochemical characteristics.[7–10] Cr(III) has low toxicity and high stability, which is beneficial to the metabolism of fat and protein in mammals.[11] Cr(III) is hundreds of times more active than Cr(VI), which is a strong carcinogen and teratogen, and could accumulate in water, animals and plants in large quantities causing catastrophic effects on the entire ecological chain and food chain.[12–16] Similarly, Fe(II) is indispensable for human life activities, and which is mainly used as important carrier for oxygen transmission by hemoglobin in human blood.[17,18] The content of Fe(III) is an important criterion for evaluating water quality, whose lack or excess will threaten the health of organisms.[19,20] At present, the methods for detecting iron and chromium ions in water mainly include ICP-MS,[21] atomic absorption spectroscopy,[22] voltammetry,[23] and fluorescence spectrophotometry.[24,25] Compared with other detection methods, the fluorescence method based on chemical sensing has the advantages of fast detection speed, high sensitivity, and simple instrument operation.[26,27]

Metal organic framework material (MOF) is a new type of inorganic–organic hybrid material with multiple functions.[28] Due to its ultra-high specific surface area and controllable pore size,[29,30] it has been widely used in catalysis, adsorption and gas storage.[31–33] In recent years, because both the inorganic and organic parts of MOF can provide a platform for generating light, the light emission caused by the metal–ligand charge transfer can increase the multi-dimensional light emitting function, the short response time, and the long luminous life.[34,35] Great progress has been made in using MOF as a fluorescence sensor to detect various metal ions.[36–39]

In this study, we chose 5-(benzimidazole-1-yl)isophthalic acid as the ligand, because the asymmetric arrangement of carboxyl groups on the conjugated benzene ring system can promote the transfer of electrons. Therefore, transition metal complexes constructed have some special fluorescence properties. Based on this, four novel complexes $[Cd(bipa)]_n$ (**1**), $\{[Zn_2(bipa)_2]\cdot 2C_2H_5OH\}_n$ (**2**), $\{[Co(bipa)]\cdot C_2H_5OH\}_n$ (**3**), $\{[Ni(bipa)_2]\cdot 2DMA\}_n$ (**4**), (H_2bipa = 5-(benzimidazole-1-yl) isophthalic acid) were synthesized under solvothermal conditions. Because of the excellent fluorescence performance of complex **1**, we initially explored its performance in detecting iron and chromium ions in water by fluorescence quenching effect.

---

[a] *School of Laboratory Medicine, Youjiang Medical University for Nationalities, Baise, 533000 Guangxi, China. E-mail: zongziao_yy@163.com; 396107666@qq.com*

[b] *College of Chemistry and Chemical Engineering, Ocean University of China, Qingdao, 266100, Shandong, China*

† Electronic supplementary information (ESI) available. CCDC 2008172, 2008119, 1911216 and 1834432. For ESI and crystallographic data in CIF or other electronic format see DOI: 10.1039/d0ra06529c

2. Experimental section

2.1 Materials and physical measurements

More detailed information on instruments and materials is listed in the ESI.†

2.2 Synthesis of $[Cd(bipa)]_n$ (1)

Complex **1** was prepared by mixing H_2bipa (0.0348 g, 0.1 mmol), $Cd(NO_3)_2\cdot 4H_2O$ (0.0308 g, 0.1 mmol) and 8 mL of DMA–H_2O (v/v = 6 : 2) stirring for 0.5 h in air. Then the solution was transformed into the Teflon-lined stainless steel vessel, sealed, heated to 130 °C for 3 days, and cooled to room temperature (5 °C h^{-1}). Colorless block crystals with a yield of 61.3% were obtained through the cooling rate of 5 °C h^{-1}. Elemental analysis (%) calcd for $C_{15}H_8CdN_2O_4$: C, 45.88; H, 2.05; N, 7.13. Found (%): C, 45.65; H, 1.98; N, 7.25. IR (KBr pellet, cm^{-1}): 1639 (s), 1558 (s), 1507 (m), 1425 (s), 1381 (s), 1241 (m), 1174 (w), 1108 (w), 1012 (w), 922 (w), 754 (s), 595 (w), 452 (m).

2.3 Synthesis of $\{[Zn_2(bipa)_2]\cdot 2C_2H_5OH\}_n$ (2)

Complex **2** was prepared by mixing H_2bipa (0.0348 g, 0.1 mmol), $Zn(NO_3)_2\cdot 6H_2O$ (0.0297 g, 0.1 mmol) and 8 mL of C_2H_5OH–H_2O (v/v = 1 : 2) stirring for 0.5 h in air. Then the solution was transformed into the Teflon-lined stainless steel vessel, sealed, heated to 130 °C for 3 days, and cooled to room temperature (5 °C h^{-1}). Light yellow transparent crystals with a yield of 67.6% were obtained. Elemental analysis (%) calcd for $C_{34}H_{28}N_4O_{10}Zn_2$: C, 52.13; H, 3.60; N, 7.15. Found (%): C, 51.98; H, 3.65; N, 7.03. IR (KBr pellet, cm^{-1}): 1659 (s), 1595 (m), 1507 (m), 1456 (m), 1397 (s), 1307 (m), 1241 (m), 1174 (w), 1055 (w), 926 (m), 750 (s), 591 (w), 532 (w), 458 (m).

2.4 Synthesis of $\{[Co(bipa)]\cdot C_2H_5OH\}_n$ (3)

A mixture of $Co(NO_3)_2\cdot 6H_2O$ (0.0291 g, 0.1 mmol), H_2bipa (0.028 g, 0.1 mmol), and 8 mL of DMA–H_2O–C_2H_5OH (v/v = 3 : 3:2) were stirred for 0.5 hour in air. And then the solution was transformed into the Teflon-lined stainless steel vessel, sealed, and heated to 110 °C for 3 days. Subsequently, the vessel was cooled to the room temperature at the degree of 5 °C h^{-1}. Violet block crystals were collected with the yield of 69.3% (based on H_2bipa). Elemental analysis (%) calcd for $C_{17}H_{14}CoN_2O_5$: C, 53.00; H, 3.66, N, 7.27%. Found: C, 53.22; H, 3.59; N, 7.36%. IR (KBr disk, cm^{-1}): 1670 (s), 1633 (s), 1500 (m), 1456 (m), 1397 (m), 1306 (w), 1240 (m), 1188 (m), 1016 (m), 904 (w), 739 (w), 626 (w), 530 (w).

2.5 Synthesis of $\{[Ni(bipa)_2]\cdot 2DMA\}_n$ (4)

The synthesis step of complex **4** was similar to that of complex **3**, only the $Co(NO_3)_2\cdot 6H_2O$ (0.0291 g, 0.1 mmol) was replaced with the $Ni(NO_3)_2\cdot 6H_2O$ (0.029 g, 0.1 mmol). The obtained green block crystals were centrifuged (yield: 54.4% based on H_2bipa). Elemental analysis (%) calcd for $C_{38}H_{34}N_6NiO_{10}$: C, 57.53; H, 4.32; N, 10.59%. Found: C, 57.39; H, 4.21, N, 10.48%. IR (KBr disk, cm^{-1}): 1675 (s), 1630 (s), 1592 (m), 1502 (m), 1458 (m), 1406 (m), 1308 (w), 1249 (w), 1183 (m), 1015 (m), 917 (m), 744 (m), 531 (m), 474 (w).

2.6 X-ray crystal structure determination

The detailed single crystal diffraction method is shown in the ESI.† Crystallographic data for the complexes are given in Table 1. Selected bond lengths and angles for the complex are listed in Table S1.† CCDC number: 2008172 for **1**, 2008119 for **2**, 1911216 for **3**, 1834432 for **4**.†

Table 1 Summary of crystal data and structure refinement parameters for **1–4**[a]

Complex	**1**	**2**	**3**	**4**
Empirical formula	$C_{15}H_8CdN_2O_4$	$C_{34}H_{28}N_4O_{10}Zn_2$	$C_{17}H_{14}CoN_2O_5$	$C_{38}H_{34}N_6NiO_{10}$
M_r	392.63	783.34	385.22	793.42
T (K)	170	170	173	173
Crystal system	Monoclinic	Monoclinic	Monoclinic	Monoclinic
Space group	$P2_1/c$	$P2_1/c$	$P2_1/c$	$C2/c$
a/Å	11.1911(4)	21.6550(6)	10.8442(14)	22.951(5)
b/Å	13.7660(4)	10.8019(3)	10.7281(14)	10.686(2)
c/Å	13.1938(4)	15.3693(4)	15.432(2)	16.444(3)
α (°)	90	90	90	90.000
β (°)	108.267(1)	108.4690(10)	108.456(3)	118.415(4)
γ (°)	90	90	90	90.000
V (Å^3)	1930.16(11)	3409.95(16)	1703.0(4)	3547.3(13)
F(000)	768	1600	788	1648
Z	4	4	4	4
R_{int}	0.0644	0.0565	0	0.072
D_{calcd} (Mg m^{-3})	1.351	1.526	1.503	1.486
Gof	1.052	1.106	1.090	1.075
Final R indices [$I > 2\sigma(I)$]	$R_1 = 0.0333$, $wR_2 = 0.0710$	$R_1 = 0.0458$, $wR_2 = 0.0954$	$R_1 = 0.0548$, $wR_2 = 0.1570$	$R_1 = 0.0513$, $wR_2 = 0.0714$
R indices (all data)	$R_1 = 0.0530$, $wR_2 = 0.0780$	$R_1 = 0.1023$, $wR_2 = 0.1169$	$R_1 = 0.0710$, $wR_2 = 0.1666$	$R_1 = 0.0928$, $wR_2 = 0.1256$

[a] $R_1 = \Sigma||F_o| - |F_c||/\Sigma|F_o|$, $wR_2 = [\Sigma w(F_o^2 - F_c^2)^2]/[\Sigma w(F_o^2)^2]^{1/2}$.

3. Results and discussion

3.1 Crystal structures of complexes 1–3

Single crystal X-ray diffraction data indicate that the complexes **1–3** belong to the monoclinic system, and space groups all are $P2_1/c$. As shown in Fig. 1a, the asymmetric unit of **1** contains one Cd(II) ion and one bipa^{2-} ligand. The central Cd(II) ion is five-coordinated, completed by one nitrogen atom (N2) and four oxygen atoms (O1A, O2B, O3C and O5D) from five individuals bipa^{2-} ligands, resulting in a slightly distorted square pyramid coordination geometry. The coordination environment of the central atoms and coordination mode of the ligand in complexes **2–3** are basically the same as in complex **1** (Fig. 1b and c). As shown in Table S1,† the Cd–N distance is 2.218(3) Å and the Cd–O distances are in the ranges of 2.208(2)–2.254(2) Å. It is interesting to note that the adjacent Cd ions are linked by four bidentate bridges from the carboxylate group of four bipa^{2-} ligands, resulted in a [$Cd_2(COO)_4$] binuclear unit with the Cd···Cd distance of 3.1972(5) Å. And each binuclear unit is encircled by six bipa^{2-} ligands and each bipa^{2-} ligand is surrounded *via* three [$Cd_2(COO)_4$] binuclear unit. Finally, a 3D framework is formed by the connection of binuclear units and the bipa^{2-} ligands (Fig. 2a). Complexes **1–3** are isostructural, which form the 3D frame structure with the same connection and growth pattern (Fig. 2b and c). Calculated by PLATON analysis, the effective free volume of **1** is 33.1% (639.2 Å^3 out of the 1930.2 Å^3 unit cell volume).

From the viewpoint of structural topology, the [$M_2(COO)_4$] (M = Cd, Zn and Co) binuclear units can be simplified to a 6-connected node in complexes **1–3**, while the "Y"-shaped bipa^{2-} ligand linked to 3 adjacent clusters can be regarded as a 3-connected nodes (Fig. 2d). The whole 3D frameworks of **1–3** can be simplified as a novel 2-nodal (6, 3)-connected topology net with $(4\cdot6^2)_2(4^2\cdot6^{10}\cdot8^3)$ topology (Fig. 2e–g). The topological analysis was produced using the TOPOS program.[40]

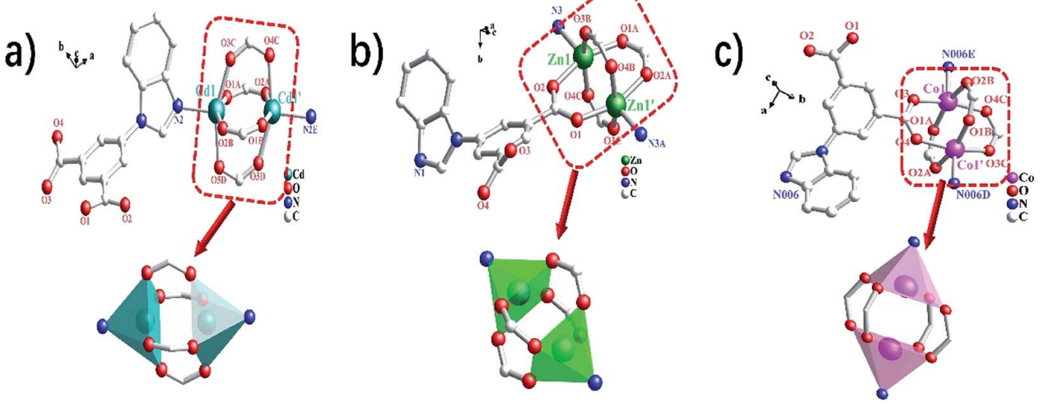

Fig. 1 (a–c) Coordination environment of the Cd(II), Zn(II) and Co(II) ions in complexes **1–3**.

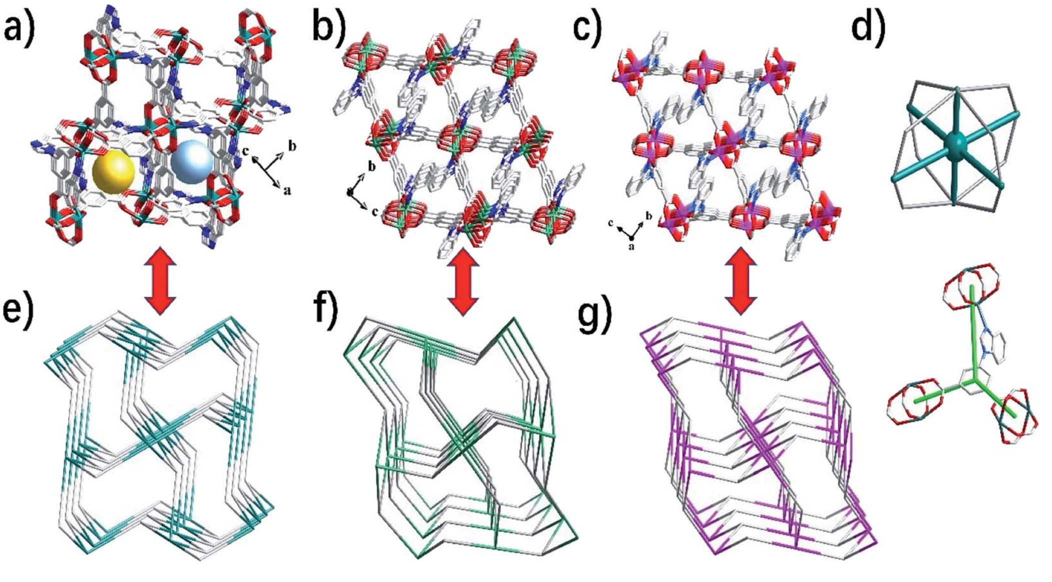

Fig. 2 (a–c) The 3D supramolecular networks of complexes **1–3**; (d) each cluster is serving as 6-connecting node while the ligand itself acting as 3-connecting node; (e–g) the topology structure of 1–3 with the point symbol $(4\cdot6^2)_2(4^2\cdot6^{10}\cdot8^3)$.

3.2 Crystal structure of $\{[\mathrm{Ni(bipa)_2}]\cdot 2\mathrm{DMA}\}_n$ (4)

Complex **4** crystallizes in the monoclinic crystal system with the *C*2/*c* space group. X-ray structural analysis shows a two-dimensional (2D) network constituted by the Ni(II) ions and the bipa^{2-} dianion. As shown in Fig. 3a, the asymmetric unit of **4** contains one Ni(II) ion, two bipa^{2-} ligands, two lattice DMA molecules. The central Ni(II) ion is hexa-coordinated, completed by two nitrogen atoms (N2A and N2B) and four oxygen atoms (O2C, O2D, O4 and O4E) from six individual bipa^{2-} ligands, resulting in a slightly distorted octahedral coordination geometry. The Ni–N distance is 2.064(2) Å, the Ni–O distances are in the ranges of 2.087(2)–2.119(2) Å (Table S1†). The distance of two adjacent Ni(II) ions is 9.3747(14), 10.2870(15) and 10.6860(21) Å separated by the bipa^{2-} ligand. As shown in Fig. 3b, the Ni(II) ions are bridged by the μ_3-bipa^{2-} to generate a 2D framework. Then the two adjacent 2D interpenetrating networks are further interconnected by the Van der Waals forces, resulting in a 2D → 3D parallel network (Fig. 3c).

From the viewpoint of structural topology, the Ni(II) ion can be simplified to a 6-connected node. The "Y"-shaped bipa^{2-} ligand can be simplified to a 3-connected node. Thus, the whole 3D framework of **4** can be simplified as a (3, 6)-connected **kgd** net with $(4^3)_2(4^6\cdot 6^6\cdot 8^3)$ topology (Fig. 3d).

3.3 Thermal analyses

To better understand the thermal stability of complexes **1–4** their thermal behaviors were performed (Fig. S2†). For complex **1**, the weight loss after 35 to 260 °C can be attributed to the loss of a small amount of DMA molecules in the guest, and the main framework begins to decompose above 400 °C. For complex **2**, below 228 °C, the 12.4% weight loss (calcd 11.7%) may be due to the removal of two ethanol molecules in the crystal lattice. When the temperature exceeds 370 °C, the frameworks of **2** begin to gradually collapse due to the oxidation of the ligands. Complex **3** displays 20.8% weight loss (calcd 11.9%), in the temperature range of 30–301 °C, results from the complete decomposition of one ethanol melecule. Because of the gradual oxidation of the organic ligands, the structural frameworks of **3** began to collapse when the temperature exceeds 410 °C. For complex **4**, the 21.4% weight loss is from 30 to 328 °C, which coincided with calcd 22.1%. This weight loss corresponds to the removal of one DMA molecule. The second weight loss corresponds to the loss of the organic ligands at 328 °C, and then the pyrolysis of the framework took place. The temperature at which the framework structure of complex **4** begins to collapse is significantly earlier than that of **1–3**, which may be caused by the coordination mode of dual-core metal being more stable than that of single-core.

3.4 Photoluminescent properties of complexes 1–4

MOFs with d10 metal centers are considered to be materials with luminescence potential.[41] The solid-state fluorescence spectra of bipa ligand and complexes **1–4** were studied at room temperature. It can be seen from Fig. S3† that the maximum fluorescence emission peak of complex **1–4** is observed at 385 nm, 392 nm, 387 nm and 395 nm, and the maximum emission peak of free bipa ligand is at 368 nm ($\lambda_{\mathrm{ex}} = 275$ nm). This can be attributed to the π^*–π and π^*–n transitions, and the fluorescence of the complex **1–4** can be considered as the fluorescence based on the bipa ligand. Compared with the emission peak of bipa ligand, **1–4** show red shifts of 17 nm, 24 nm, 19 nm and 27 nm, respectively. The red shift may be caused by ligand-to-metal charge transfer (LMCT).[42]

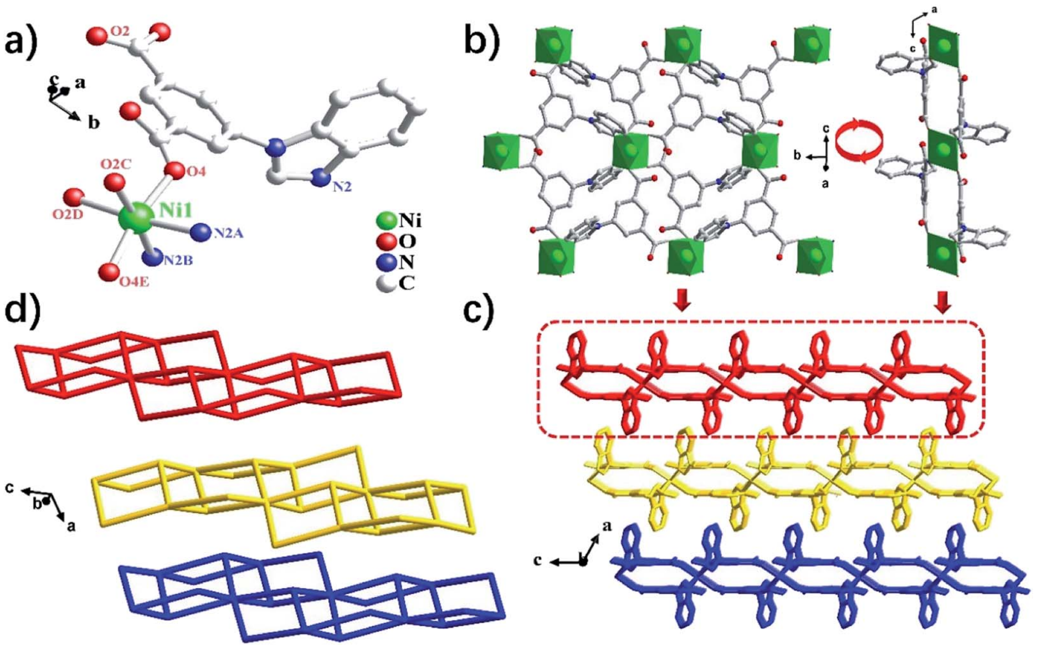

Fig. 3 (a) Coordination environment of the Ni(II) ions in **4**; (b) view of the 2D network; (c) view of the 2D → 3D supramolecular networks of **4**; (d) the topology structure of 4 with the point symbol $(4^3)_2(4^6\cdot 6^6\cdot 8^3)$.

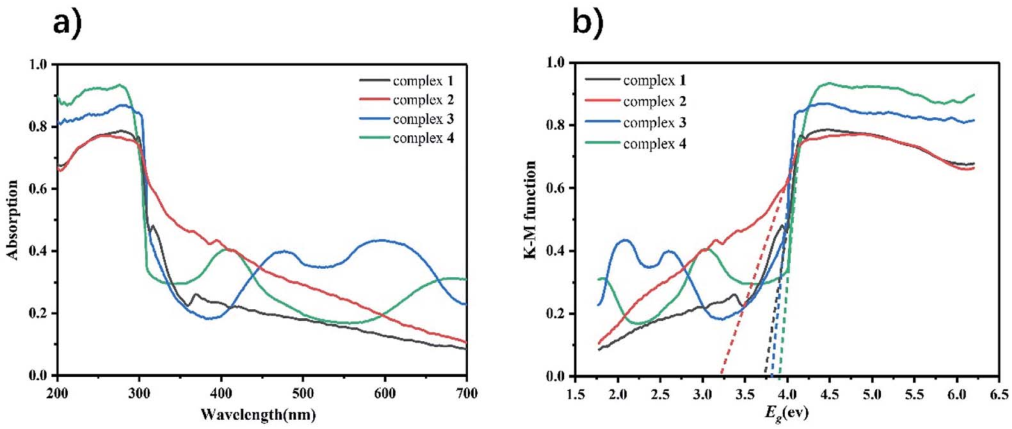

Fig. 4 (a) UV-vis diffuse reflectance spectra of complexes **1–4**; (b) Kubelka–Munk-transformed diffuse reflectance spectra of complexes **1–4**.

3.5 Optical properties of complexes 3–4

It is well known that the optical band gap is one of the reference standards for measuring whether MOFs have potential photocatalytic properties. Herein, the optical absorption and diffuse-reflection spectrum of complexes **1–4** were measured at ambient temperature. As depicted in Fig. 4, the solid-state UV spectrum of complexes **1–4** showed the maxima absorption at 280 nm, 255 nm, 278 nm and 275 nm, respectively. The energy band gaps of complexes **1–4** can be calculated according to the formula: $E_g = 1240/\lambda$ (where λ is the wavelength and E_g is the band energy gap). The E_g of complexes **1–4** obtained by extrapolation of the linear portion of the absorption edges were estimated to be 3.72 eV, 3.20 eV, 3.87 eV and 3.81 eV.

3.6 Pore characterization and stability test of complex 1

The porosity of complex **1** was tested by N_2 adsorption and desorption at 77 K (Fig. 5a). The results show that the isotherm is a type IV adsorption isotherm, and the hysteresis loop belongs to the H3 type in the IUPAC classification. The hysteresis loop is closed at a relative pressure of 0.71. By the Brunauer–Emmett–Teller (BET) method, the specific surface area of complex **1** is 47.8 m^2 g^{-1}, and the average pore diameter is 4.5 nm. By comparing the PXRD patterns before and after the experiments of sensing Fe^{3+}, $Cr_2O_7^{2-}$ and CrO_4^{2-}, it can be judged that the complex **1** maintains the structural integrity and good phase purity (Fig. 5b).

3.7 Detection of Fe^{3+}

Based on the excellent fluorescent properties of complex **1**, we explored **1** as a selective and sensitive fluorescent probe to detect metal ions in water. 3 mg of powder samples of complexes **1** were added to 5 mL of $FeCl_2$ and MNO_x solutions with the concentration of 1 mM (M = K^+, Ca^{2+}, Co^{2+}, Mn^{2+}, Mg^{2+}, Li^+, Zn^{2+}, Ni^{2+}, Al^{3+}, Hg^{2+}, Ag^+, Cu^{2+} and Fe^{3+}), sonicated for 15 min to obtain a stable suspension, and then detected their fluorescence intensities. As shown in Fig. S4,† compared with the aqueous solution of complex **1**, the complex solutions with different metal cations show a certain degree of fluorescence quenching. In the solution of Fe^{3+}, the fluorescence intensities of complex **1** were completely quenched. In order to avoid the accidental results of the experiment, three repeated

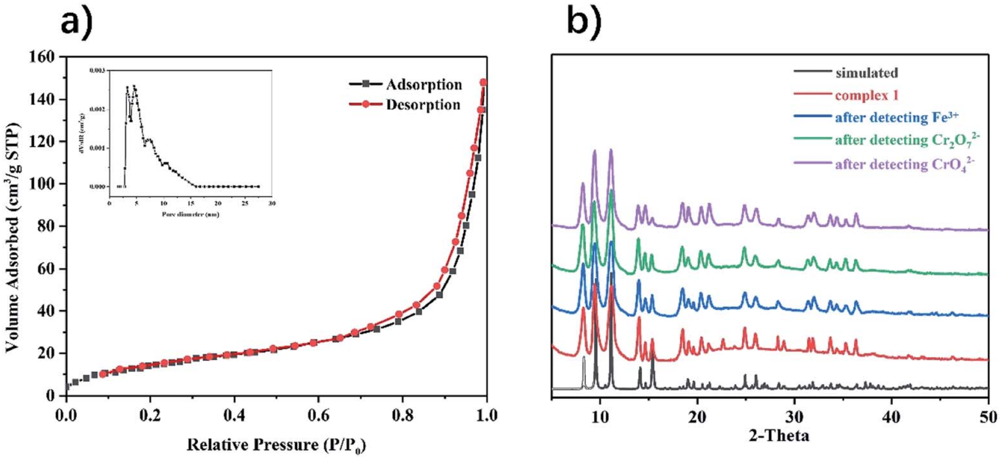

Fig. 5 (a) Nitrogen adsorption and desorption isotherms for complex **1**; (b) PXRD spectra of complex **1** before and after detection.

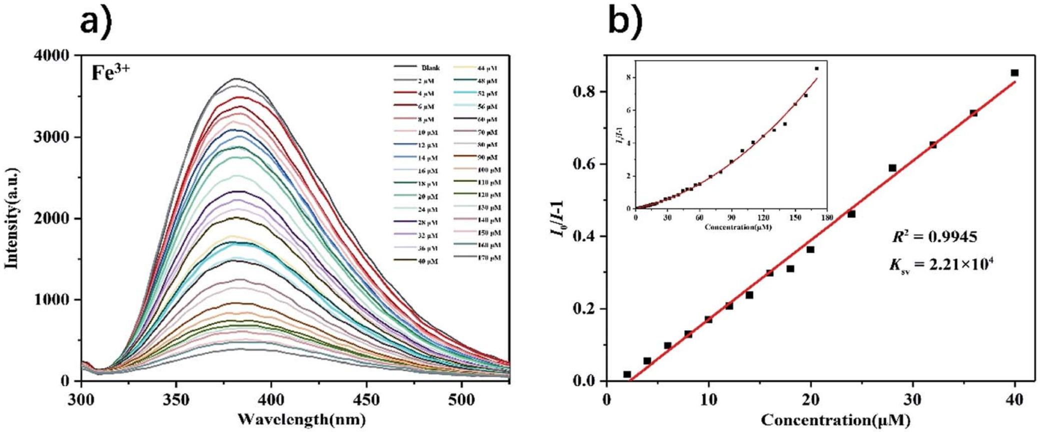

Fig. 6 (a) Fluorescence spectra of complex **1** in the presence of various concentrations of Fe^{3+} ($\lambda_{ex} = 275$ nm); (b) S–V plot of complex **1** upon incremental addition of Fe^{3+} ions.

experiments showed that it is still complex **1** that exhibits the highest fluorescence quenching efficiency in the solution of Fe^{3+} (97.8%). The fluorescence quenching abilities of metal ions solutions to complex **1** are in turn: $Fe^{3+} > Cu^{2+} > Ag^{+} > Hg^{2+} > Al^{3+} > Ni^{2+} > Fe^{2+} > Zn^{2+} > Li^{+} > Mg^{2+} > Mn^{2+} > Co^{2+} > Ca^{2+} > K^{+}$.

To further investigate the sensitivity of complex **1** in detecting Fe^{3+}, that is, the effect of concentrations of Fe^{3+} on the fluorescence intensity of **1**, aqueous solutions of different concentrations of Fe^{3+} were prepared. As concentrations of Fe^{3+} gradually increased, the fluorescence intensities of the complex **1** decreased (Fig. 6). In addition, the fluorescence quenching constant of **1** can be calculated using the Stern–Volmer equation: $I_0/I - 1 = K_{sv}[M]$ (where, I_0 is the fluorescence intensity of complex in water, I is the fluorescence intensity of complex in the solution with a certain concentration of ion, [M] is ion concentration, K_{sv} is quenching constant).[43] It can be calculated that in the low concentration range of 0–40 μM, there is a good linear relationship between the fluorescence intensity of **1** and the concentration of Fe^{3+} ($R^2 = 0.9945$), and the quenching constants K_{sv} are 2.21×10^4 M^{-1}. K_{sv} is comparable to other fluorescent MOFs of the same type used to detect Fe^{3+}, which makes complex **1** a competitive candidate (Table S2†). The limit of detection of **1** was calculated as 1.36×10 μM by the equation $LOD = 3\sigma/K_{sv}$ (σ is the standard deviation of 5 blank experiments for the fluorescence intensity of complex **1**). Fluorescence titration experiments were also performed on other metal ions in the range of 0 to 100 μM, the experimental results showed that the effect of changes in the concentrations of other metal ions on the fluorescence intensity of complex **1** is negligible (Fig. S5–S16†). In all metal ions, Fe^{3+} showed the highest fluorescence quenching efficiency to complex **1** at different concentrations (Fig. 7). Those results indicated that complex **1** has good selectivity and high sensitivity in detecting Fe^{3+}.

In the detection of iron ions in actual water samples, interference by other metal ions is inevitable. Therefore, the anti-interference performance of iron ions coexisting with other metal ions in water is evaluated by measuring the fluorescence intensity of complex **1** in the mixed metal ion solution. In the presence of 100 μM interfering ions, the decrease in the fluorescence intensity of complex **1** is negligible (Fig. S17†). It is

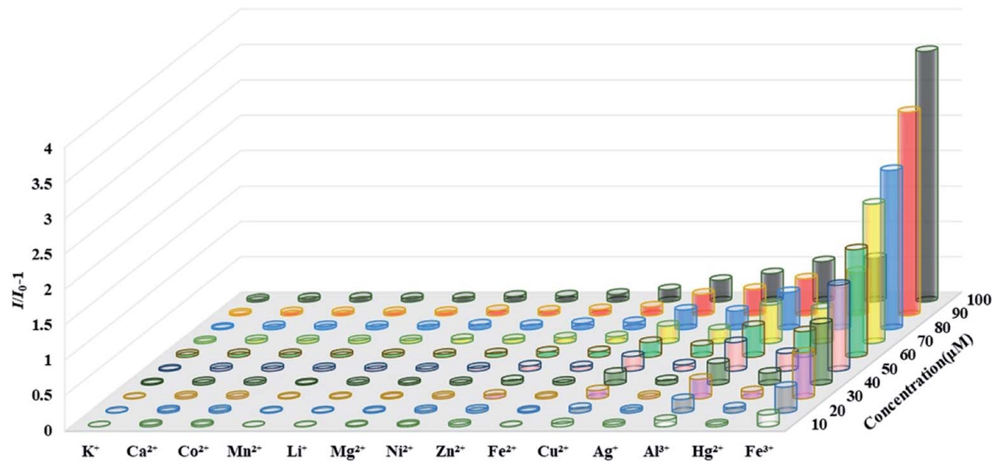

Fig. 7 Fluorescence responses of complex **1** towards different kinds of mate ions (0–100 μM).

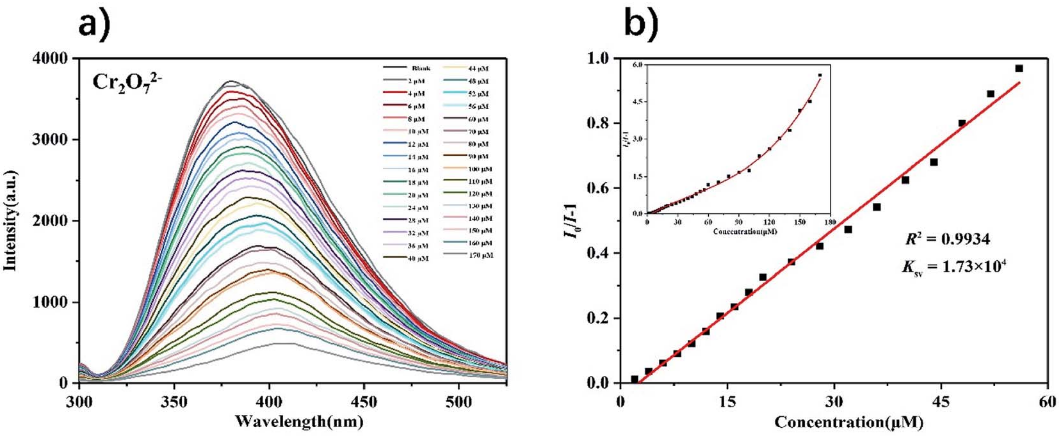

Fig. 8 (a) Fluorescence spectra of complex **1** in the presence of various concentrations of $Cr_2O_7^{2-}$ ($\lambda_{ex} = 275$ nm); (b) S–V plot of complex **1** upon incremental addition of $Cr_2O_7^{2-}$.

worth noting that after adding the equivalent of iron ions, the fluorescence intensity decreases sharply. Those results clearly showed that complex **1** can be used as a fluorescent probe to sensitively and selectively detect iron ions in water, and the influence of the presence of other interfering mate ions can be ignored. As can be seen from Fig. S18a,† the fluorescence intensity of complex **1** reached a stable level in about 8 s after adding different concentrations of Fe^{3+}, which indicated that the complex **1** can quickly identify Fe^{3+}. After each fluorescence experiment of detecting Fe^{3+}, the solution was centrifuged, the complex **1** powder was washed with ethanol and DMF, and activated for the next experiment. The blank fluorescence intensity of complex **1** after centrifugal, washing and activation can be recovered to the original intensity. After five experiments, the blank fluorescence intensity of complex **1** only decreased by 8.6%, and the quenching efficiency was almost unchanged after adding iron ions (Fig. S18b†). This means that complex **1** can be reused by simply cleaning and activating after each test, which is an important property of functional materials.

3.8 Detection of $Cr_2O_7^{2-}$and CrO_4^{2-}

Next, we explored the performance of complex **1** as a fluorescent probe to recognize anions in water. Since complex **1** has the highest fluorescence intensity in the solution of K^+ ion, 3 mg of complex **1** powder was dispersed in 5 mL of a series of potassium salt solutions with the concentration of 1 mM (Cl^-, I^-, NO_3^-, SO_4^{2-}, ClO_3^-, IO_3^-, $H_2PO_4^-$, SCN^-, $Cr_2O_7^{2-}$ and CrO_4^{2-}). As shown in Fig. S19,† the fluorescence intensities of complex **1** were completely quenched in solutions of $Cr_2O_7^{2-}$ and CrO_4^{2-}, while only slight changes in other anion solutions. The fluorescence titration experiment of complex **1** detecting $Cr_2O_7^{2-}$ and CrO_4^{2-} were completed by recording the intensities of the fluorescence response of complex **1** after gradually increasing the concentrations of anions. The experiment result shows that as the concentrations of $Cr_2O_7^{2-}$ and CrO_4^{2-} gradually increased, the fluorescence intensities of complex **1** decreased accordingly (Fig. 8 and 9). From the Stern–Volmer equation (*vide supra*), the quenching constants for $Cr_2O_7^{2-}$ and CrO_4^{2-} in the concentration range of 0–60 µM are 1.73×10^4 M^{-1} and 1.63×10^4 M^{-1} respectively. Compared with other MOFs with the

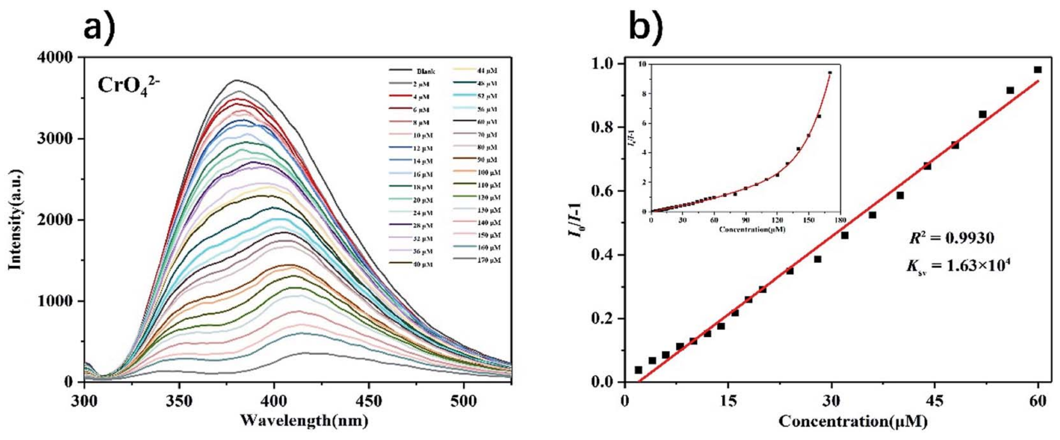

Fig. 9 (a) Fluorescence spectra of complex **1** in the presence of various concentrations of CrO_4^{2-} ($\lambda_{ex} = 275$ nm); (b) S–V plot of complex **1** upon incremental addition of CrO_4^{2-}.

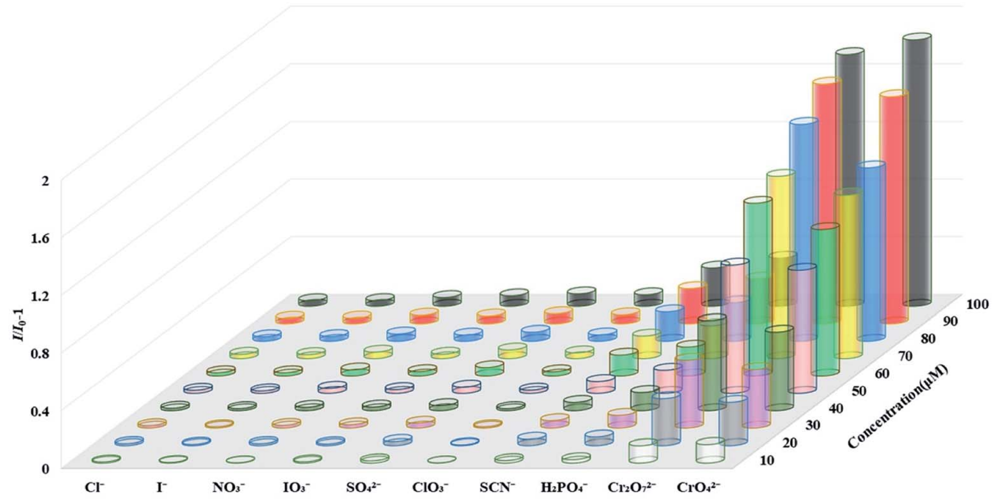

Fig. 10 Fluorescence responses of complex **1** towards different kinds of anions (0–100 μM).

same function, complex **1** has an advantage in detecting $Cr_2O_7^{2-}$ and CrO_4^{2-} in water (Table S2†). Fluorescence titration experiments were carried out in other anion solutions, the fluorescence intensities of complex **1** changed very little within 100 μM concentrations (Fig. S20–S27†). Compared to other anion solutions, complex **1** showed the highest quenching efficiency in solutions of $Cr_2O_7^{2-}$ and CrO_4^{2-} at different concentrations (Fig. 10).

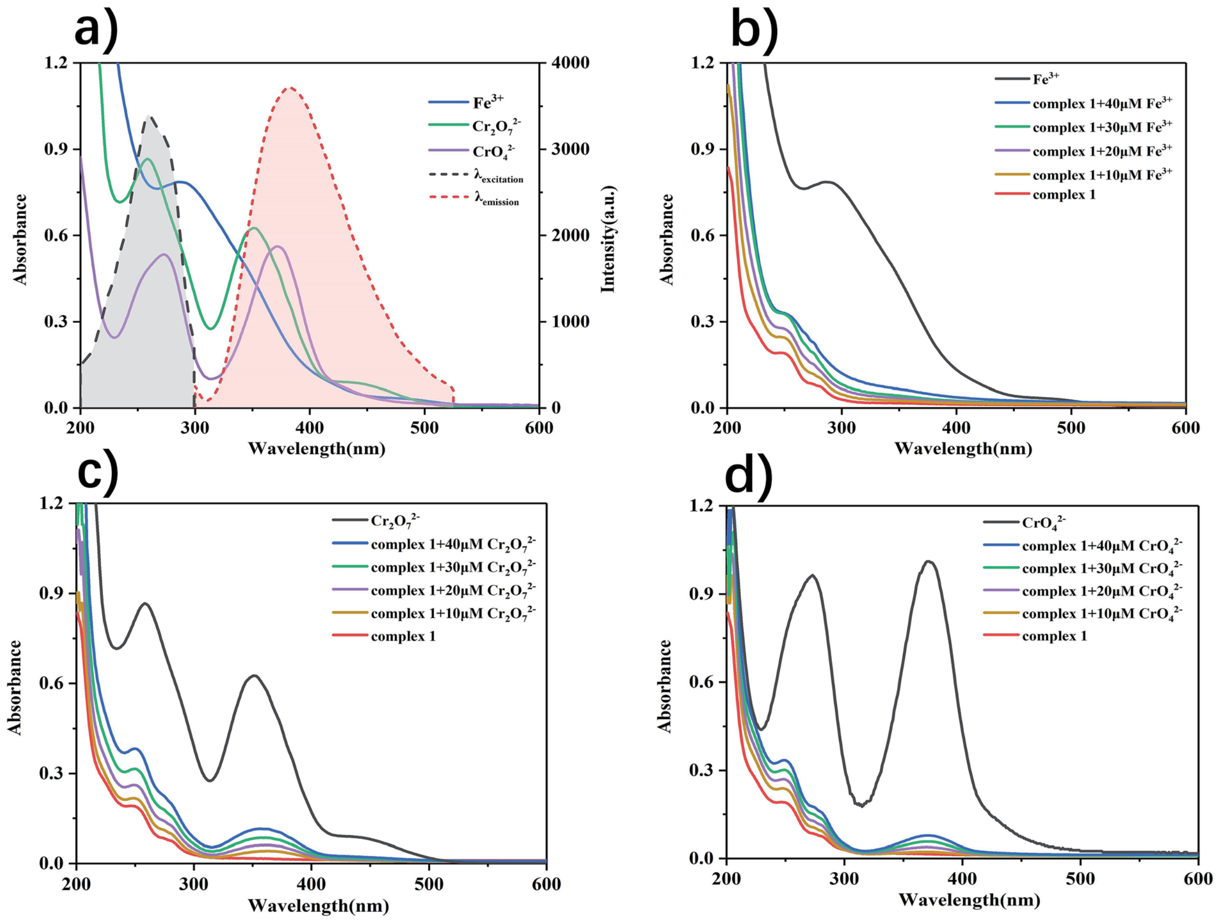

Fig. 11 (a) Spectral overlap between UV-vis absorption spectra of different ions (Fe^{3+}, $Cr_2O_7^{2-}$, and CrO_4^{2-}) and emissions as well as the excitation spectrum of complex **1**; UV-vis absorption spectra of 1 upon addition of different concentrations of (b) Fe^{3+}; (c) $Cr_2O_7^{2-}$; (d) CrO_4^{2-}.

Similarly, the interference of other competing anions in the detection of $Cr_2O_7^{2-}$ and CrO_4^{2-} in water is inevitable. Taking $Cr_2O_7^{2-}$ as an example, the anti-interference study of hexavalent chromium ion was carried out. After adding 100 μM of competitive anion solutions, the fluorescence intensities of complex **1** changed little, and then decreased significantly after adding an equivalent solution of $Cr_2O_7^{2-}$ (Fig. S28†). From Fig. S29a,† the fluorescence intensity of complex **1** reached a stable level in about 13 s after adding different concentrations of $Cr_2O_7^{2-}$. Follow the same procedure as above to recover and reuse the complex **1** for the detection of hexavalent chromium ion. After five cycles of experiments, the fluorescence intensity of complex **1** only decreased by about 10%, and the quenching efficiency after adding the solution of $Cr_2O_7^{2-}$ was still nearly 100% (Fig. S29b†). The above experimental results basically verify that the complex has high selectivity, high sensitivity and reusability for detecting hexavalent chromium ions in water.

3.9 Sensing mechanism

The mechanism by which Fe^{3+}, $Cr_2O_7^{2-}$ and CrO_4^{2-} causes the fluorescence quenching of complex **1** may be as follows. By comparing the FT-IR spectrum of the original complex **1** and that recovered from the suspension containing Fe^{3+}, $Cr_2O_7^{2-}$ and CrO_4^{2-}, it shows that there is no obvious change (Fig. S30†). Which indicated that the framework structure of the complex **1** remains intact, and there is no chemical bonding during this process. Moreover, the resonance energy transfer between analyte and complex promotes fluorescence quenching.[44] Ultraviolet absorption spectra of metal ions and anions were measured (Fig. S31†). The result is that there are large overlaps between the fluorescence emission spectrum of complex **1** and UV absorption spectra of Fe^{3+}, $Cr_2O_7^{2-}$ and CrO_4^{2-}, and there is almost no overlap with other ions (Fig. 11a).

Therefore, Fe^{3+}, $Cr_2O_7^{2-}$ and CrO_4^{2-} exhibited the strongest absorption of the emission light of complex **1**. In order to further verify this mechanism, UV absorption titration experiments revealed that there was significant absorption enhancement by gradually adding the concentrations of Fe^{3+}, $Cr_2O_7^{2-}$ and CrO_4^{2-} to complex **1** (0–40 μM). As can be seen from Fig. 11b–d, a rapid and significant increase in absorption was observed due to the increased absorption after the addition of Fe^{3+}, $Cr_2O_7^{2-}$ and CrO_4^{2-}, the excitation light of complex **1** was weakened, resulting in fluorescence quenching. Thus, the high selectivity and sensitivity quenching response of complex **1** to Fe^{3+}, $Cr_2O_7^{2-}$ and CrO_4^{2-} should be attributed to resonance energy transfer.

4. Conclusions

In summary, we synthesized four novel metal–organic frameworks $[Cd(bipa)]_n$ (**1**), $\{[Zn_2(bipa)_2]\cdot 2C_2H_5OH\}_n$ (**2**), $\{[Co(bipa)]\cdot C_2H_5OH\}_n$ (**3**), $\{[Ni(bipa)_2]\cdot 2DMA\}_n$ (**4**). Complexes **1–2** exhibit potential fluorescent properties. Fluorescence experiments show that complex **1** has a good application prospect for the detection of Fe^{3+}, $Cr_2O_7^{2-}$ and CrO_4^{2-} in water with high selectivity and sensitivity.

Conflicts of interest

There are no conflicts to declare.

Acknowledgements

This work was supported by the Fundamental Research Funds for the Guangxi Natural Science Foundation Program (Grant No. 2019GXNSFBA245086).

References

1 B. Saha and C. Orvig, *Coord. Chem. Rev.*, 2010, **254**, 2959–2972.
2 K. H. Cheung and J.-D. Gu, *Int. Biodeterior. Biodegrad.*, 2007, **59**, 8–15.
3 J. G. Sandana Mala, D. Sujatha and C. Rose, *Microbiol. Res.*, 2015, **170**, 235–241.
4 P. Sun, Z.-T. Liu and Z.-W. Liu, *Ind. Eng. Chem. Res.*, 2009, **48**, 6882–6889.
5 J. Barnhart, *Regul. Toxicol. Pharmacol.*, 1997, **26**, S3–S7.
6 D. Park, Y.-S. Yun, J. Y. Kim and J. M. Park, *Chem. Eng. J.*, 2008, **136**, 173–179.
7 B. Qiu, C. Xu, D. Sun, Q. Wang, H. Gu, X. Zhang, B. L. Weeks, J. Hopper, T. C. Ho, Z. Guo and S. Wei, *Appl. Surf. Sci.*, 2015, **334**, 7–14.
8 E. Agrafioti, D. Kalderis and E. Diamadopoulos, *J. Environ. Manage.*, 2014, **133**, 309–314.
9 Y. Ma, W.-J. Liu, N. Zhang, Y.-S. Li, H. Jiang and G.-P. Sheng, *Bioresour. Technol.*, 2014, **169**, 403–408.
10 H. Gu, S. B. Rapole, J. Sharma, Y. Huang, D. Cao, H. A. Colorado, Z. Luo, N. Haldolaarachchige, D. P. Young, B. Walters, S. Wei and Z. Guo, *RSC Adv.*, 2012, **2**, 11007–11018.
11 K. Choi, S. Lee, J. O. Park, J.-A. Park, S.-H. Cho, S. Y. Lee, J. H. Lee and J.-W. Choi, *Sci. Rep.*, 2018, **8**, 1438.
12 A. D. Dayan and A. J. Paine, *Hum. Exp. Toxicol.*, 2001, **20**, 439–451.
13 S. A. Katz and H. Salem, *J. Appl. Toxicol.*, 1993, **13**, 217–224.
14 P. Rani, A. Sharma, A. Husain, G. Kumar, H. Kaur, K. K. Bhasin and G. Kumar, *CrystEngComm*, 2019, **21**, 7447–7459.
15 G. Kumar, R. Guda, A. Husain, R. Bodapati and S. K. Das, *Inorg. Chem.*, 2017, **56**, 5017–5025.
16 S. Mitra, A. Sarkar and S. Sen, *Nanotechnol. Environ. Eng.*, 2017, **2**, 11.
17 T. Hirayama, *Free Radicals Biol. Med.*, 2019, **133**, 38–45.
18 J. Wang and K. Pantopoulos, *Biochem. J.*, 2011, **434**, 365–381.
19 X.-H. Zhou, L. Li, H.-H. Li, A. Li, T. Yang and W. Huang, *Dalton Trans.*, 2013, **42**, 12403–12409.
20 C.-X. Yang, H.-B. Ren and X.-P. Yan, *Anal. Chem.*, 2013, **85**, 7441–7446.
21 W. Huang, J. Jiao, M. Ru, Z. Bai, H. Yuan, Z. Bao and Z. Liang, *Sci. Rep.*, 2018, **8**, 8603.
22 W.-S. Zhong, T. Ren and L.-J. Zhao, *J. Food Drug Anal.*, 2016, **24**, 46–55.

23 S. K. Mittal, S. Rana, N. Kaur and C. E. Banks, *Analyst*, 2018, **143**, 2851–2861.
24 K. Qu, J. Wang, J. Ren and X. Qu, *Chem.–Eur. J.*, 2013, **19**, 7243–7249.
25 J. Li, Q. Wang, Z. Guo, H. Ma, Y. Zhang, B. Wang, D. Bin and Q. Wei, *Sci. Rep.*, 2016, **6**, 23558.
26 A. Valizadeh, H. Mikaeili, M. Samiei, S. M. Farkhani, N. Zarghami, M. Kouhi, A. Akbarzadeh and S. Davaran, *Nanoscale Res. Lett.*, 2012, **7**, 480.
27 X. Wei, Z. Zhang and Z. Wang, *Microchem. J.*, 2019, **145**, 55–58.
28 O. M. Yaghi, M. O'Keeffe, N. W. Ockwig, H. K. Chae, M. Eddaoudi and J. Kim, *Nature*, 2003, **423**, 705–714.
29 H.-C. J. Zhou and S. Kitagawa, *Chem. Soc. Rev.*, 2014, **43**, 5415–5418.
30 H. Furukawa, N. Ko, Y. B. Go, N. Aratani, S. B. Choi, E. Choi, A. Ö. Yazaydin, R. Q. Snurr, M. O'Keeffe, J. Kim and O. M. Yaghi, *Science*, 2010, **329**, 424.
31 J. L. C. Rowsell and O. M. Yaghi, *J. Am. Chem. Soc.*, 2006, **128**, 1304–1315.
32 D. A. Reed, D. J. Xiao, M. I. Gonzalez, L. E. Darago, Z. R. Herm, F. Grandjean and J. R. Long, *J. Am. Chem. Soc.*, 2016, **138**, 5594–5602.
33 Y. S. Wei, M. Zhang, R. Zou and Q. Xu, *Chem. Rev.*, 2020, DOI: 10.1021/acs.chemrev.9b00757.
34 Z. Xiang, C. Fang, S. Leng and D. Cao, *J. Food Drug Anal.*, 2014, **2**, 7662–7665.
35 S. Dang, E. Ma, Z.-M. Sun and H. Zhang, *J. Mater. Chem.*, 2012, **22**, 16920–16926.
36 B. B. Rath and J. J. Vittal, *Inorg. Chem.*, 2020, **59**, 8818–8826.
37 Y. Liu, Y. K. Lu, B. Zhang, L. Hou and Y. Y. Wang, *Inorg. Chem.*, 2020, **59**, 7531–7538.
38 C. H. Liu, Q. L. Guan, X. D. Yang, F. Y. Bai, L. X. Sun and Y. H. Xing, *Inorg. Chem.*, 2020, **59**, 8081–8098.
39 C. Xu, C. Bi, Z. Zhu, R. Luo, X. Zhang, D. Zhang, C. Fan, L. Cui and Y. Fan, *CrystEngComm*, 2019, **21**, 2333–2344.
40 V. A. Blatov, A. P. Shevchenko and D. M. Proserpio, *Cryst. Growth Des.*, 2014, **14**, 3576–3586.
41 Z.-Q. Shi, Z.-J. Guo and H.-G. Zheng, *Chem. Commun.*, 2015, **51**, 8300–8303.
42 G.-Z. Liu, L.-Y. Xin and L.-Y. Wang, *CrystEngComm*, 2011, **13**, 3013–3020.
43 B. Zhu, Z. Zong, X. Zhang, D. Zhang, L. Cui, C. Bi and Y. Fan, *Appl. Organomet. Chem.*, 2020, **34**, e5518.
44 S. Chen, Z. Shi, L. Qin, H. Jia and H. Zheng, *Cryst. Growth Des.*, 2017, **17**, 67–72.